Tensor network methods for quantum-inspired image processing and classical optics

Nicolas Allegra*
Thales Alenia Space, Cannes
(Dated: October 28, 2025)

Tensor network methods strike a middle ground between fully-fledged quantum computing and classical computing, as they take inspiration from quantum systems to significantly speed up certain classical operations. Their strength lies in their compressive power and the wide variety of efficient algorithms that operate within this compressed space. In this work, we focus on applying these methods to fundamental problems in image processing and classical optics such as wave-front propagation and optical image formation, by using directly or indirectly parallels with quantum mechanics and computation. These quantum-inspired methods are expected to yield faster algorithms with applications ranging from astronomy and earth observation to microscopy and classical imaging more broadly.

I. INTRODUCTION

For decades, scientists have tried to simulate quantum systems on classical computers. The challenge lies in the exponential memory needed, making direct simulations unfeasible for anything beyond very small systems or idealized systems. To overcome this, researchers had spent decades developing clever approximations for quantum and statistical lattice systems. Although tensor networks—particularly matrix product states—can be traced back to R.J Baxter and his work on the corner transfer matrix method for solving 2d statistical mechanics problems [1], their popular emergence occurred decades later in the nineties, with the major breakthrough of S.R. White's density matrix renormalization group algorithm [2], which compress quantum systems by retaining only the most relevant correlations.

Recently, the field of tensor networks has seen a surge in interest due to their connections to quantum computing. Quantum researchers use tensor networks to design and simulate their quantum machines, while tensor networks experts borrow ideas from quantum theory to emulate and compete with quantum performance [3–7]. This feedback loop benefits both sides and benefits also scientists and engineers tackling complex real-world problems. To name a few examples, tensor networks have enabled immediate applications in machine learning [8, 9], fluid mechanics [10–14], finance [15], electromagnetism [16], material science [17] and computational chemistry [18].

One of the first application of tensor networks outside of physics was an interesting study on image compression using matrix product states [19]. Although this 20-year-old paper did not have a significant impact on the field of image processing at the time, the rapidly growing field of quantum machine learning has recently revived interest in this topic [20, 21]. In the present work, we build upon these earlier studies by applying some of these quantum computing and tensor network compression ideas to image processing and Fourier optics.

*Electronic address: nicolas.allegra@gmail.com

Outline of the paper In the first half of this paper, we focus on natural images and quantum-inspired methods for encoding them into quantum-like objects, which will prove useful for many applications. Several types of matrix product encodings will be compared with one another, along with alternative tensor network structures such as tree tensor networks. The discussion will then shift to classical operations on images represented as tensor network operators, and how these can be applied to classical imaging and image processing. One of the goals of this paper is to draw parallels between Fourier optics and quantum mechanics, and to use these parallels to construct efficient approximations of classical optical propagation in very large dimensions by finding local Hamiltonians whose evolution represents these classical operations. These connections will be often made using ideas stemming from quantum computation—even though no quantum computers are involved—showing how quantum mechanics concepts can lead to efficient classical computations.

II. NATURAL IMAGES AND QUANTUM ENCODINGS

We define a continuous "image" (sometimes called a scene or an objet) as the intensity h of an electromagnetic field of a classical object on a 2d plane. From this function of continuous variables, we can consider an approximation on a 2d grid of size $L \times L = 2^n \times 2^n$ by evaluating it at discrete points $(x,y) = \left(\frac{a}{2^n}, \frac{b}{2^n}\right)$ with $a,b \in \{0,1,2,...,2^n-1\}$. As we can not get access to a real continuous image of the physical world (or a model of it), we will have to settle for a digital image as a proxy to the real world and try to separate what comes from the physical scene to what comes from the measurement device (the digital camera here). The question we are interested in here, is how much information and correlation is relevant in an image at the continuous limit and how this can used to compress efficiently the image as well as implement faster optical and imaging simulations on classical computers.



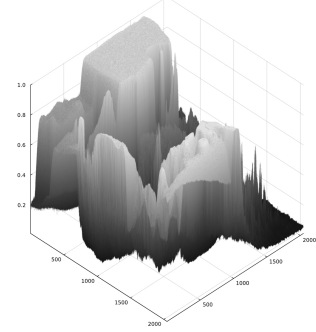


FIG. 1: A black and white picture and its height field representation. This picture will be used throughout this paper.

Natural images are closer to real physical systems that they are from random samples of a generic distribution, moreover they are known to be scale invariant with a power spectrum that obeys a power-law distribution [22, 23]. In a more recent study [21], the authors showed that, over a large dataset of various natural images of various shapes and forms, the behavior of the Fourier amplitudes follows $\langle \hat{h}(k_x, k_y) \rangle \sim \mathcal{O}(k_x^{-1.1}) \mathcal{O}(k_y^{-1.07})$. In this present work, we choose to work with a single "statistically average" image [58] (cf. Fig. 1) that is very representative of the power-law behavior of natural images. The picture showed numerous times in this paper follows this behavior honorably well (it is actually closer to $\hat{h}(k) \sim k^{-1}$) and saves us from the time/resource consuming task of averaging over a large dataset of images, with all the generalization and statistical limitations that it entails.

Next, we are mapping this matrix to a higher dimensional objet (a tensor) and then operate compression within this space. The first tensor image encoding that we are considering comes from the field of quantum machine learning, where researchers are interested in efficient ways to feed data to quantum computers. The so-called Flexible Representation of Quantum Images (FRQI) [24] is a quantum encoding scheme that non-trivially represents images by a multi-qubit quantum state $|h\rangle$. More precisely, an image of size $2^n \times 2^n$ is encoded using a normalized superposition of 2n+1 qubits

$$|h\rangle = \frac{1}{2^n} \sum_{i=0}^{2^{2n}-1} |c(x_i)\rangle \otimes |i\rangle, \tag{1}$$

with $|c(x_i)\rangle = \cos\left(\frac{\pi}{2}x_i\right)|0\rangle + \sin\left(\frac{\pi}{2}x_i\right)|1\rangle$, where x_i encodes the intensity of the pixel at position i (see Fig. 2),

and the basis state $|i\rangle$ represents the pixel's position in the image. Usually, a row by row flattening of the matrix is used, but more complex paths (see [25] for an application of Hilbert curve to quantum systems) such as Hilbert, Peano or Moore curves can be used [59]. In-

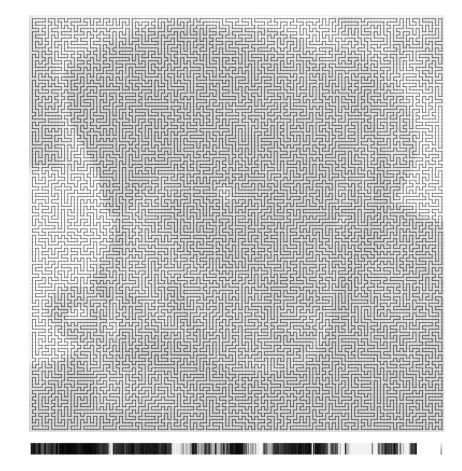


FIG. 2: Matrix to vector reshaping. Below the image, the corresponding vector noted x_i with $i = 0...2^{2n-1}$.

tuitively, the path should be as compact as possible such that local correlations in the image remain local upon transformation. In the following, we will use mostly Hilbert curve encoding or will specified otherwise. This encoding allows for efficient quantum image processing by parallel manipulation of all pixel values through unitary operations on the quantum state. This way, we only need 2n + 1 qubits to store the information of 2^{2n} grayscale pixel values, which is an exponential reduction to the classical case. Although this encoding requires one more qubit that other encodings, it has been shown to work the best on natural images [21].

Thanks to the multi-scale nature of typical images, an other interesting and relevant way of encoding images into tensor is the so-called quantics representation [27, 28] (first appeared in the quantum computing community [19, 29, 30]) for the tensors as it naturally encodes scale separation. Each component can be thus written as a rank-2 tensor. In 2d, this means splitting the indices cor-

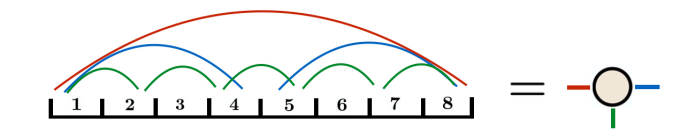


FIG. 3: Quantics representation of the linear grid L=8. Let us denote h_{ijk} the resulting tensor. In this example, we have $x_1 \to h_{000}, x_2 \to h_{100}...,x_7 \to h_{111}$ and $x_8 \to h_{001}$.

^[58] As a remark, although the use of "Lena" as the go-to image in the field of image processing has, understandably so, fallen out of favor in recent years for many reasons, its non-power-law behavior could be added to the list of grievances.

^[59] In Fig. 2, for illustration purpose, a self-avoiding walk is generated by a pivot algorithm [26]

responding to spatial coordinates x and y in their binary components $(x^1x^2x^3...x^n)_2$ and $(y^1y^2y^3...y^n)_2$ and rearranging them to form new tensor indices $\mu_p = (x^py^p)_2$. This yields a 2n order tensor $h^{\mu_1\mu_2...\mu_n}$ where each μ_p corresponds to a particular length scale. [60] Technically a full tensor of the form $h^{\mu_1\nu_1\mu_2\nu_2...\mu_n\nu_n}$ contains $2^n \times 2^n$ parameters, as many as the initial matrix we are considering, only in a different tensor shape. A non-trivial decomposition of this tensor into an interconnected network might reduce the number of parameters from an exponentially to (in the best cases) a logarithmically small number. This generic approach applied to our original image is illustrated in Fig. 4.

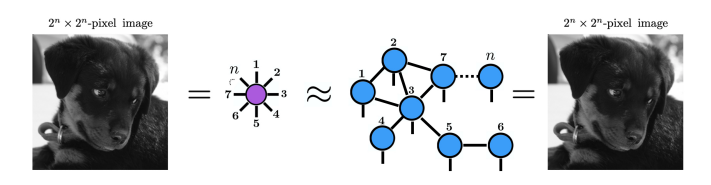


FIG. 4: Tensor network compression of an image. Here, a generic tensor network is showed for the sake of generality. The approximate symbol will quantify the precision of the compression.

This tensor network decomposition could be used as a way of compressing images for transmission and storage or, as we will see later, as a crucial step in a pipeline of transformations allowing to outperform standard optical simulations or image processing. Many different topologies of tensor networks [31–33] have been proposed over the years and became very powerful theoretical and numerical tools that allow to capture complex phenomena regularly found in the fields of condensed matter, high-energy physics or quantum computation [34, 35]. In the following section, we focus on the two most common topologies of tensor networks, namely matrix product states and tensor trees and evaluate their compressive capabilities.

III. MATRIX PRODUCT STATES AND TENSOR TREE NETWORKS

The specific tensor network we are focusing on first, is called a matrix product state (MPS) in the physics literature or a tensor train (TT) in the mathematical community. The matrix decomposition outlined below (see Fig. 5) is a generalization of the singular value decomposition and can be used to decompose a generic tensor into constituent tensors of lower order. Once the image is encoded into a tensor network, the numerical evaluation

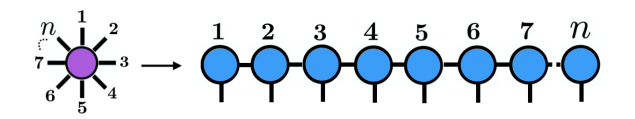


FIG. 5: Illustration of the decomposition of high-order tensor into a matrix product state. The arrow represents a sequential singular value decomposition.

of the compressive power versus the reconstruction error is measured and the total number of parameters in the network is called the total dimension D. Now, we apply the decomposition to the picture showed earlier and analyze the error of the decomposition with respect to the original image for increasing allowed rank and increasing size. For evaluation sake, we downsize the original image to increasing sizes with an interpolating algorithm to simulate an image with increasingly higher resolutions. The goal is to mirror what we would have done with a typical stat-mech system, by studying the rank of the MPS for various sizes and analyze the large-scale thermodynamic limit.

Let us define the mean squared error between the original image and the decompressed image as

$$\epsilon(L) = \frac{1}{L^2} \sum_{ij} (h_{ij} - \tilde{h}_{ij})^2. \tag{2}$$

Additionally, we introduce the inverse compression ra-

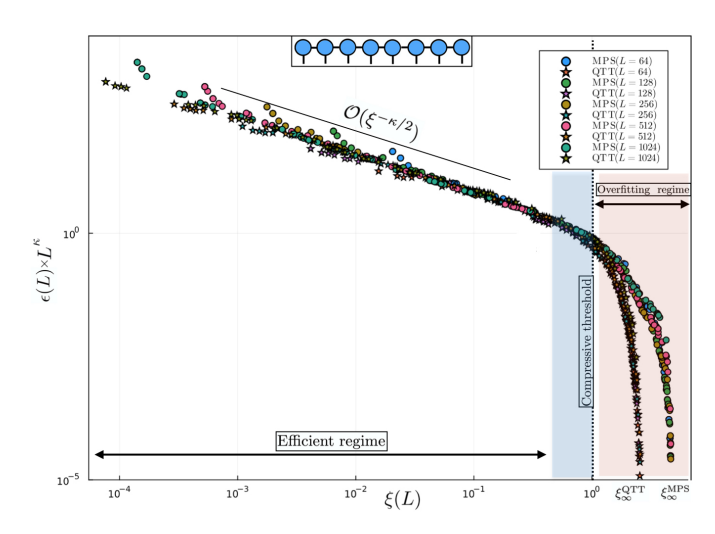


FIG. 6: Scaling of the mean squared error of the compression depending on system size for Hilbert curve MPS and quantics tensor trains (qTT).

tio as $\xi(L) = DL^{-2}$, which is the relevant order parameter for this approximation. Numerical simulations (see Fig. 6) on qubit encoding matrix product states and quantics tensor trains suggest the following finite-size scaling

$$\epsilon(L) = L^{-\kappa}\phi(\xi). \tag{3}$$

^[60] As an example the value of the image h at coordinate (x,y)=(43,78) on a grid of size L=128 is given by the tensor component $h^{00101011001110}$

with $\phi(\xi) \sim \xi^{-\alpha}$ with $\alpha \approx 0.75$ and $\kappa \approx 1.5$ for $\xi \ll 1$. In this efficient regime $\epsilon(L) \sim \mathcal{O}(1)$, meaning that the error is (modulo multiplicative logarithmic corrections) independent of system size (consistent with [21]), and results are fairly similar between the two encodings. Conversely, the compression ratio at fixed error increases polynomially $\epsilon = C^{0.75} \times L^{1.5}$, so $C(L) \sim L^2[61]$.

In the overfitting regime, the error goes to zero exponentially quickly at a value $\xi \to \xi_{\infty}$. We notice that $\xi_{\infty}^{q\text{TT}} < \xi_{\infty}^{\text{MPS}}$ by a big margin (because there is one less qubit needed in the quantics representation than FRQI). This is due to the fact that, by construction of the singular value decomposition, the dimension of a random MPS of n sites is $D_{\text{max}}(n) = 8/3 \times 2^n$ so $\xi_{\infty}^{q\text{TT}} = 8/3$ and $\xi_{\infty}^{\text{MPS}} = 16/3$ and at very high resolution the error is mostly dominated by pixel noise in the image [62]. Interestingly, the value of ξ_{∞} is also of certain relevance in the intermediate regime (blue region in Fig. 6) near the compressive threshold $\xi = 1$ since a smaller value ξ_{∞} seems to force the curve to accelerate faster towards this line. This fact allows the qTT to improve over the Hilbert MPS in this intermediate region. This argument will be made more clear in the following section.

Another important decomposition is the tree tensor network (TTN) where the constituent tensors of the network lie on the nodes of a connected acyclic tree graph. The appeal of tensor tree network comes down to their relative ease of constructions and contractions as well as their greater expressive power and has been recently explored in the context of multivariate function approximations [36]. Two typical examples of trees are pictured below (see Fig. 7). In Fig. 8, we plot the scaling of $\xi(L)$

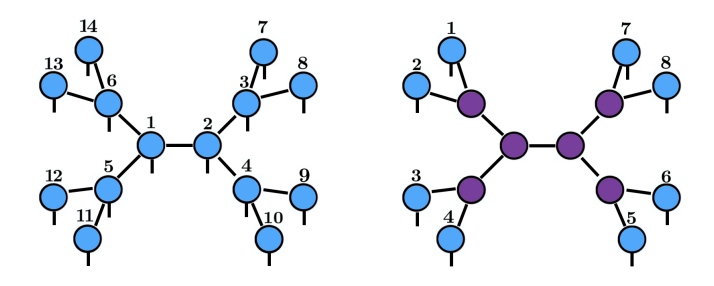


FIG. 7: Left Binary tensor tree network with 14 physical sites. Right Binary tensor network tree with 8 boundary sites.

for boundary tensor trees and observe a similar scaling as before. In quantum many-body physics, it is common knowledge that matrix product states can efficiently represents 1d quantum systems with area-law entanglement, meaning it can capture only short-range correlations. In

contrast, the hierarchical structure of tensor trees can also describe more complex types of entanglement, including some long-range quantum correlations, in higher-dimensional or critical systems where entanglement scaling can exceed that of an area law. In the scenario that we are interested in, the image considered follows an area law (since the bond dimensions of the MPS remain constant up to quite a large precision), and tensor trees only marginally improve the compression ratio but not the scaling of the function $\xi(L)$.

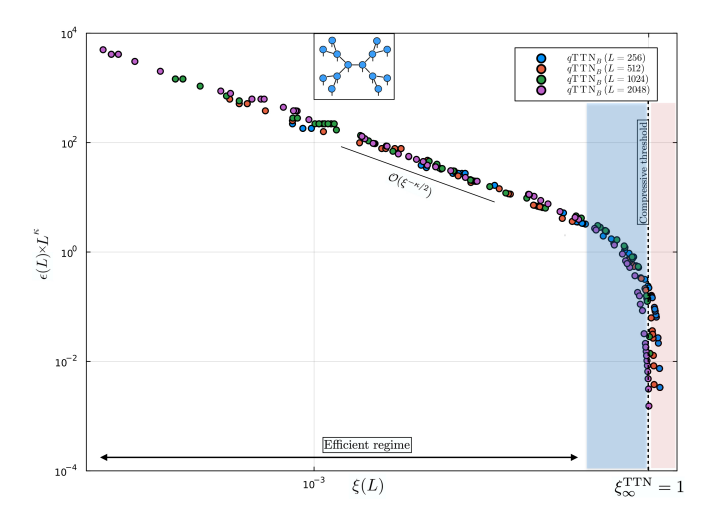


FIG. 8: Scaling of the error with the system size for $qTTN_B$.

Nevertheless, it is clear that the error goes to zero rather differently due to the maximal number of parameters allowed by the SVD in these kinds of networks. We can show that a large n, maximally random tensor tree has at most 2^n parameters. We take the example of the boundary binary tree (see right Fig. 7), the maximal number of parameter is $D_{\max}(n) = n(2 \times 2) + \sum_{k=1}^{\log_2(n)-2} \frac{n}{2^k} \left(2^{2^{k+1}-2} \times 2^{2^{k+1}-1}\right) + 2 \times 2^{n-2}$. The first term $n(2 \times 2)$ corresponds to the n outside branch tensors and the last term corresponds to the two central tensors. The largest term inside the sum is $2^n - 1$ so $D_{\text{max}}(n) = 4n + 2^{n-1} + 2 \cdot 2^{n-2} = 2^n + 4n$, implying a value (up to a tiny $\mathcal{O}(n)$ term) of $\xi_{\infty}^{\text{TTN}} = 1$ for large n. A similar counting operation can be done for bulk tensor trees, and would have lead to the same result. It means that in the thermodynamic limit, in contrast to matrix product states, TTN always act as a compressor ($\xi < 1$) regardless of the level of approximation which is already an interesting fact on its own. Therefore, tensor trees offer greater compressive power in the intermediate regime (see Fig. 8), as the number of parameters approaches the compression limit with increasing system size.

This is illustrated in the table below, where tensor trees clearly outperform MPS and continue to compress the image even for very small reconstruction error, whereas MPS fail to do so. We expect this behavior to be generic in average and not specific to this particular image. Although comparisons with standard image compression

^[61] This is in sharp contrast with local compressors like JPG, since they possess a maximum compression ratio which is given by the division of the original image in small finite-size squares

^[62] A more fondamental question is whether or not a real image of the physical world (not a digital picture) would be admit a true area-law at any reasonable scale.

Tensor Nets and encodings	$\epsilon = 10^{-3}$	$\epsilon = 10^{-4}$	$\epsilon = 10^{-5}$
MPS (SARW)	270	1.46	0.48
MPS (S)	320	2.24	0.46
MPS (H)	330	4.1	0.64
qTT	352	4.2	0.72
$q TTN_B$	370	10.2	2.3

TABLE I: Compression ratio for several errors with L=2048. The three firsts tensor nets use FRQI with respectively a random walk (SARW), snake-like (S) and a Hilbert curve (H) path encoding. The fourth is the quantics tensor train and the last is a quantics encoding on a bulk tensor tree. Tensor trees manage to still be compressive (last column) even for very small errors, whereas MPS do not.

algorithms are not showed here, we mention that tensor networks might have a big advantage at very large size and relative high error. A comprehensive benchmark—although beyond the scope of this paper—on the performance of tensor networks across large datasets of diverse images would be necessary to rigorously demonstrate their relative strengths and weaknesses. The last section of this work will be devoted to optical applications that could be significantly sped up using this formalism.

IV. IMAGE PROCESSING AND IMAGE FORMATION

Many geometric operations on images, such as shifts, rotations and scale transformations can be represented efficiently by tensor network operators of small and fixed rank. In the case of MPS (TTN), the operators are appropriately named matrix product operators (tree tensor operators). Those objects are tensor networks that can act on other tensor networks (see Fig. 9). The complexity of the contraction MPS/MPO (TTN/TTO) depends strongly of the rank of the two objects $\mathcal{O}(2n\chi_1^2\chi_2^2)$. This favorable scaling allows for very efficient operations that would have been very costly otherwise. Similarly, im-

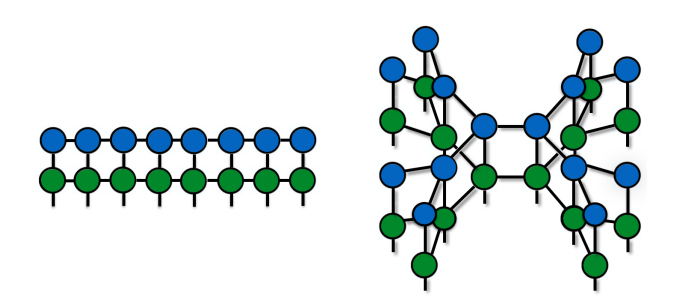


FIG. 9: Operations on images as MPS/MPO contraction on the left and TTN/TTO contraction on the right. The takeaway message is that theses contractions can be done very efficiently.

age transforms such as the Hadamard transform, discrete

Fourier transform or the discrete sine/cosine transforms can also be constructed very efficiently in this formalism. Quantum mechanically speaking, it means that the equivalent quantum circuit does not create a lot of entanglement among the qubits, a weakly entangled initial state $|\phi\rangle$ propagating into the circuit would result in another (perhaps even more) weakly entangled state $|\psi\rangle$.

A trivial (but still useful) example of operator with specific applications in image processing and compression is the previously mentioned Hadamard transform. The Hadamard matrix of order 2^n , denoted H_n , can be defined recursively using the tensor product

$$H_1 = \frac{1}{\sqrt{2}} \begin{pmatrix} 1 & 1 \\ 1 & -1 \end{pmatrix}, \qquad H_n = H_1 \otimes H_{n-1} \quad \text{for } n \ge 2.$$

Equivalently, it can be written as a unitary operator \hat{U} on the space of qubits such that [63]

$$\hat{U} = H_1^{\otimes n} = \left(\frac{\hat{X} + \hat{Z}}{\sqrt{2}}\right)^{\otimes n},\tag{5}$$

which is by definition a matrix product operator of rank 1 in terms of Pauli gates. Classically, the Hadamard transform can be computed in $L\log L$ operations, using the fast Hadamard transform algorithm. With tensor networks (or a quantum computer, as it is a quantum logic gate that can be parallelized) it would take $\mathcal{O}(1)$ time. Because of the trivial structure, the Hamiltonian \mathcal{H} and the evolution operator $(\mathcal{H} \propto \mathbb{I} - \hat{U})$ are the same up to a phase. Explicitly, the MPO governing the unitary evolution reads

$$\hat{U} = \sum_{\substack{a_1, \dots, a_n = \{0,1\}\\b_1, \dots, b_n = \{0,1\}}} \left(\prod_{i=1}^n W_{a_i b_i}^{[i]} \right) \left| \mathbf{a} \right\rangle \left\langle \mathbf{b} \right|,$$

where the local tensors

$$W_{a_i b_i}^{[i]} = H_1 \delta_{\alpha_{i-1}, 1} \delta_{\alpha_i, 1}, \tag{6}$$

are of order (2,2,1,1). The same local tensors can be similarly plugged on a tree tensor network such as shown in Fig. 9. Applying the Hadamard transform to an image approximated by an MPS or TTN is simply the application of a Hadamard gate to each qubit individually. This suggests that some image processing tasks or optical calculations that can be expressed as tensor operators might be significantly faster than more standard classical methods. Complex Hadamard matrices in general cannot be written as Eq. (5), and a description in terms of MPO would surely lead to an exponential increase in

^[63] In this paper, we choose the notation quantum computation notation $\{\hat{X}, \hat{Y}, \hat{Z}\}$ instead of $\{\hat{\sigma}_x, \hat{\sigma}_y, \hat{\sigma}_z\}$ for the Pauli matrices.

bond dimensions. As a counter point, although the discrete Fourier transform is a particular case of complex Hadamard matrices, it has been shown that the quantum Fourier transform operator can be written explicitly as a matrix product operator with a finite rank χ and error $\epsilon = \mathcal{O}(n \mathrm{e}^{-\chi \log(\chi/3)})$ [37, 38]. The last section of this article will be devoted to optical applications of such speed-ups.

In the following, we shall see how to incorporate the previous results into a realistic optical system. The simplest of calculations is to compute the point spread function of a classical optical system that contains phase aberrations. A monochromatic coherent field can be expressed as the plane wave

$$E(r,\theta) = A(r,\theta)e^{-ik\Phi(r,\theta)},$$
(7)

where $k=2\pi/\lambda$, $A(r,\theta)$ is the amplitude of the wavefront describing the intensity variations and $\Phi(r,\theta)$ is the phase function, which captures the optical path difference and aberrations of the optical system. Phase aberration $\Phi(r,\theta)$ is often expanded using Zernike polynomials $\Phi(r,\theta) = \sum_{n,m} c_n^m Z_n^m(r,\theta)$, where $Z_n^m(r,\theta)$ are the Zernike polynomials, and c_n^m are the corresponding coefficients representing different aberrations like defocus, astigmatism, and coma. The focal plane amplitude distribution is obtained from the Fraunhofer diffraction integral (see the standard textbook [39])

$$E_{\rm f}(u,v) = \int r \mathrm{d}r \int \mathrm{d}\theta E(r,\theta) \mathrm{e}^{-ikr(u\cos\theta + v\sin\theta)}, \quad (8)$$

where (u, v) are spatial coordinates in the focal plane, and $A(r, \theta)$ is the pupil function, typically a circular aperture. The point spread function is simply given by

$$PSF(u, v) = |E_f(u, v)|^2,$$
 (9)

which is the intensity of the field at the focal plane.

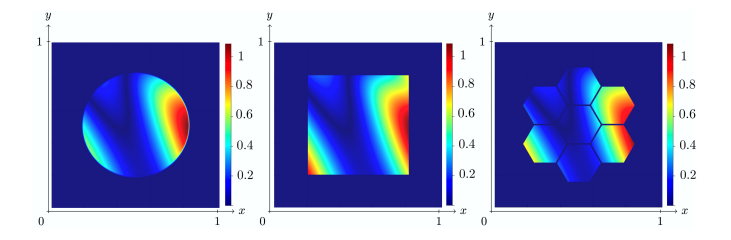


FIG. 10: Three classic apertures considered for the simulations plus a continuous phase field living on them. The middle case will be surprisingly easy to approximate with MPS while the others will turn up to be more difficult.

The classical Fraunhofer propagation of the continuous field E_0 can be seen as a unitary propagation of a non-normalized quantum state $|\phi\rangle$ living in the Hilbert space of infinitely many qubits. The non-unitary operation that computes the PSF of the optical system is, in this context, defined by the non-unitary process of quantum measurement. Mathematically, it boils down to the

following dictionnary

$$E_0 \leftrightarrow |\phi\rangle,$$
 (10)

$$\mathcal{F}\{\bullet\} \leftrightarrow \hat{U}_{\text{qft}} = \hat{U}_{\text{qft}}^{(x)} \otimes \hat{U}_{\text{qft}}^{(y)}, \tag{11}$$

$$E_{\rm f} \leftrightarrow |\psi\rangle = \hat{U}_{\rm qft}|\phi\rangle,$$
 (12)

$$PSF \leftrightarrow |PSF\rangle = \frac{|\psi\rangle|\psi\rangle^{\dagger}}{|\langle\psi|\psi\rangle|^2}.$$
 (13)

As said earlier, a low-rank matrix product operator construction of the QFT has recently been developed and could be implemented here. To take advantage of this MPO formulation, the field $|\phi\rangle$ requires also a low-rank form. A summary of the calculation steps is illustrated in Fig. 11.

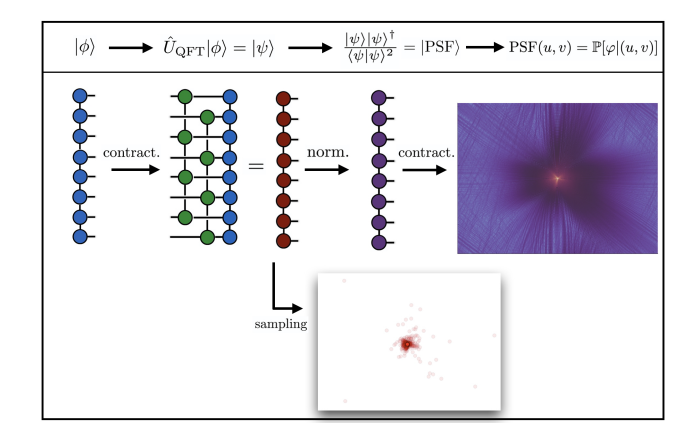


FIG. 11: Schematic representation of the tensor construction of the PSF computed with the circular aperture showed in Fig. 10. The Fourier MPO is applied twice, first in the x then y direction.

Contrary to the standard PSF calculation, the matrix product state formulation allows photon sampling (see Fig. 11) without ever computing the photon statistical distribution, *ie.* the PSF. The perfect sampling algorithm can be used to sample from this distribution [40, 41]. As the name suggests, the algorithm draws perfect samples form photon distribution and is very efficient as it scales as $\mathcal{O}(\chi^2)$ for a properly right-orthogonalized MPS. This method can be especially useful in situations in which photon statistical behavior needs to be taken into account.

In this section, we want to approximate the continuous function $E(r,\theta)$ by a matrix product state $|\phi\rangle$, without executing the exponentially expensive operation that is exhaustively storing the function on a grid $L \times L$. To overcome this limitation, we then adopt a sampling-based approach exploiting the family of tensor-cross interpolations algorithms. In particular, we focus on the method described in [42, 43], which is based on the LU decomposition. The algorithm we employ takes the input, represented as a function, and generates an approximated tensor in the quantics MPS form. The final tensor is obtained by deterministically sampling the initial one, with

a linear number of calls $\mathcal{O}(n\chi^2)$, depending on the rank of the function.

We now proceed to approximate the amplitude $A(r, \theta)$ with a quantics tensor train. For our simulations, we chose three relevant geometries a very favorable, a very unfavorable and a fairly middle of the road (see Fig. 10) in order to identify the pros and cons of these methods. The problem of discretizing a circular discontinuous function is already discussed in Fernandez et al [43], they showed that the bond dimension increases along the tensor train as $\chi_p \sim 2^{n/2}$ with a maximum bond dimension of $\chi_{\rm max} \sim 2^{2(n+1)/3}$. This behavior is correct for the exact discontinuous function but the bond dimension can be reduced by using a smoother function with a parameter dictating the smoothness of the discontinuity. For the following numerical simulations we choose a continuous function $A(r, \theta) = (1 + \alpha^{-1} \exp((r - r_0)^2))^{-1}$ with $\alpha = 0.001$ and $r_0 = 0.5$. In addition, we will also consider the two other geometries of Fig. 10, namely a simple box function $A(r,\theta) = box(x,y)$ and a segmented aperture $A(r,\theta) = \operatorname{Hex}(x,y).$

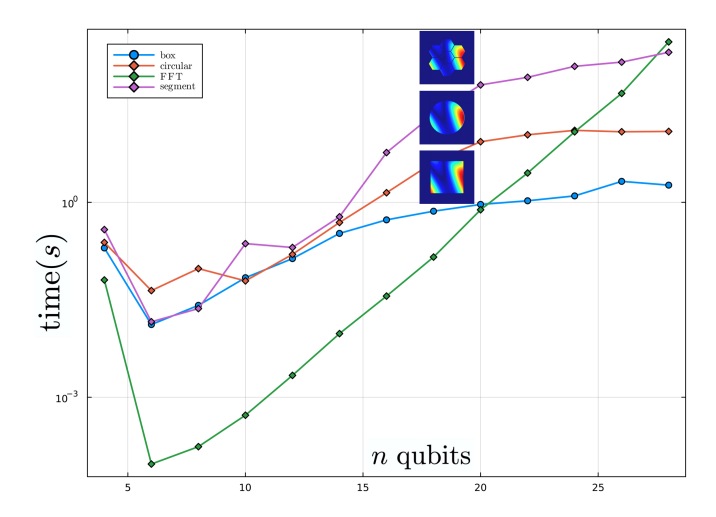


FIG. 12: Run times of Eq. (10) for the three apertures showed in Fig. 10 compared to the FFT computation in green.

It can be argued that since the Zernike polynomials also live on the aperture, the maximum bond dimension is somehow dominated by the discontinuity, regardless of the number of modes considered. The numerical experiment (see Fig. 12) shows run times of Eq. (10) for the three apertures shown earlier. Times are measured for several grid sizes defined by the number of qubits and are compared to a standard FFT calculation. In logarithmic time, it indicates that the run times for the MPS/MPO formulation are (up to log corrections) constant, with a constant depending on the complexity of $|\psi\rangle$, while the FFT computation scales linearly with system size.

For an extended scene $I_{\rm obj}$, the image formed in the focal plane is given by the convolution of the scene with the point spread function. Mathematically, this is expressed as $I_{\rm img} = I_{\rm obj} * {\rm PSF}$. In the Fourier domain, this convolution simplifies to a multiplication $\hat{I}_{\rm img}(f_x, f_y) =$

 $\hat{I}_{\text{obj}}(f_x, f_y) \cdot \hat{PSF}(f_x, f_y)$, where \hat{I} and \hat{PSF} are the Fourier transforms of the object and \hat{PSF} , respectively. The function \hat{PSF} is also known as the optical transfer function, which characterizes how different spatial frequencies are transmitted by the optical system. The extended scene I_{obj} can also be seen as a state $|S\rangle$ such that the final image state reads

$$I_{\rm img} = I_{\rm obj} * {\rm PSF} \rightarrow \hat{U}_{\rm iqft} (\hat{U}_{\rm qft} | {\rm PSF}) \times \hat{U}_{\rm qft} | {\rm S}).$$
 (14)

The algorithm used to perform the calculation of element-wise multiplication scales as $\mathcal{O}(d\chi^3)$, a faster algorithm [44] could be implemented to speed things up. Evaluating this process for a finite number of qubits $n=2\log_2(L)$ is exactly equivalent to the exact calculation on a finite grid of size $L\times L$ by matrix multiplication and fast Fourier transform (FFT). An implementation is showed in the plot below (see Fig. 13). We plot the run times versus a classical FFT implementation for comparisons for increasing approximation error ϵ . The difference in scaling is similar to the simpler case of the PSF computation.

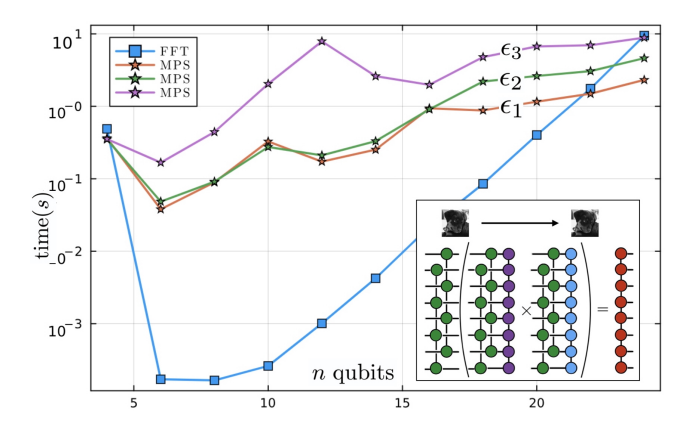


FIG. 13: Run times of the matrix product image formation for increasing precisions versus the standard FFT implementation. The MPS/MPO construction is showed on the bottom right and the circular aperture is used.

In this formalism, the entire image formation chain can be computed efficiently, with varying levels of complexity depending on the source image, aperture, and aberrations. In addition, other components of realistic systems—such as polarization, detector modulation functions, and even noise—can also be incorporated. As the name suggests, Fourier optics is heavily based on the fact that classical optics becomes computationally faster in Fourier space as convolutions become multiplications. In the following section we will exploit this feature in more depth and apply it to other optical propagations.

V. WAVE OPTICS AND QUANTUM MECHANICS

Interestingly, many other optical propagators might be good candidates for finite-rank MPO approximations, as they often respect strict conditions of smoothness, locality and symmetry. Previously we have considered the far-field regime described by the Fraunhofer propagation (the Fourier transform), a similar analysis can be generalized to the near-field regime, namely the Fresnel propagation which is valid for small distance of propagation $(z \ll D)$ in the paraxial approximation, and more generally to the free propagation at any distance.

A. Free optical propagation

In full generality, we are considering here the angular spectrum transfer function which can accurately simulate propagation at any distance z. It describes the free homogenous propagation of a monochromatic optical field $E_z(x,y)$ over a distance z in the frequency domain. It is given by

$$\tilde{T}_z(f_x, f_y) = \exp\left(2i\pi z \sqrt{\frac{1}{\lambda^2} - f_x^2 - f_y^2}\right),$$
 (15)

where f_x , f_y are the spatial frequencies in the x and y directions, λ is the wavelength of the wave and z is the propagation distance. This propagator is the solution of the Green function of the following Helmholtz equation

$$\left(\frac{\partial^2}{\partial z^2} + \nabla_\perp^2\right) E_z + k^2 E_z = 0. \tag{16}$$

In the following, we fix $\lambda = 633nm$ and $\Delta x = \Delta y = 10\mu m$ for all numerical simulations.

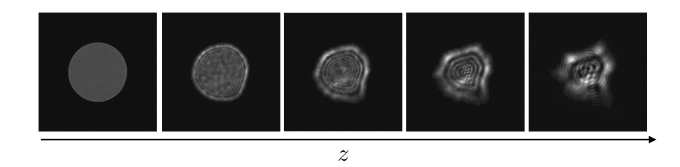


FIG. 14: Angular spectrum propagation Eq. (15) of an aberated wave-front for increasing distance z.

To simulate wave propagation, the field is transformed into the frequency domain $\tilde{E}_0(f_x,f_y)=\mathcal{F}\{E_0(x,y)\}$. The field at distance z is then given by $\tilde{E}_z(f_x,f_y)=\tilde{E}_0(f_x,f_y)\cdot T_z(f_x,f_y)$. For evanescent components, where $f_x^2+f_y^2>1/\lambda^2$, the square root becomes imaginary. The real space propagator that transform E_0 into E_z is then described a unitary operator (see Fig. 15). As a warm-up exercise, before tackling the more difficult task of systematically constructing low-rank matrix product operators for optical propagators, we first employ a brute-force method (computationally infeasible for large n) to diagnose the structure of these operators. In Fig. 16, we show how to construct MPO's by SVD in a similar fashion we used for MPS previously. The propagator Fig. 15 described as a MPO \hat{U}_{AS} , can not be written as separable operator $U^{(x)} \otimes U^{(y)}$ because of the square root in

$$\mathcal{F}^{-1}(\hat{H}_z\mathcal{F}(\bullet)) \longrightarrow \hat{U}_{\mathrm{AS}} = \underbrace{\begin{array}{c} 2^{n/2} & \chi & 2^{n/2} \\ 2^{n/2} & \chi & 2^{n/2} \end{array}}_{2^{n/2}}$$

$$\mathcal{F}^{-1}(\hat{H}_z^{\mathrm{Fresnel}}\mathcal{F}(\bullet)) \longrightarrow \hat{U}_{\mathrm{Fresnel}}^{(x)} \otimes \hat{U}_{\mathrm{Fresnel}}^{(y)} = \underbrace{\begin{array}{c} 2^{n/2} & \chi = 1 \\ 2^{n/2} & \chi = 1 \end{array}}_{2^{n/2}} \underbrace{\begin{array}{c} 2^{n/2} & \chi = 1 \\ 2^{n/2} & \chi = 1 \end{array}}_{2^{n/2}}$$

FIG. 15: Tensor representation of the optical propagators

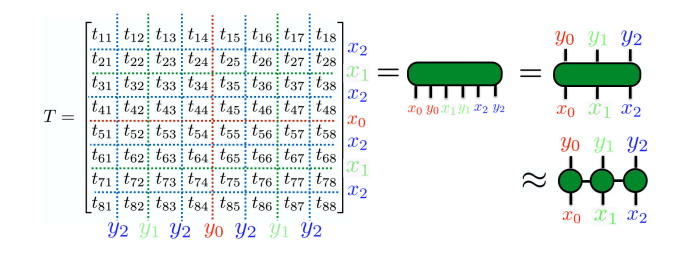


FIG. 16: Interleaved construction of a matrix product operator from a matrix. The construction is similar to the quantics MPS, only the placement of the indices are different.

Eq. (15) causing couplings between the frequencies. The amount of coupling (entanglement) can nevertheless be quantify by organizing the transfer function into a matrix product operator with a fused representation and looking at the rank between the two halves of the operator (see Fig. 17). We observe that the full angular spectrum op-

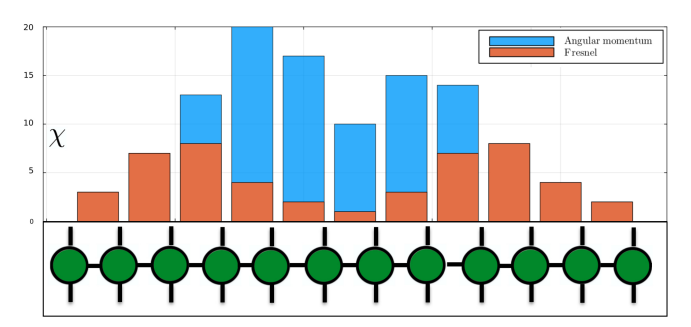


FIG. 17: Bond dimensions along a chain of 12 qubits for the 2d Fresnel and 2d ASTF matrix product operators in a fused representation. In this setting, the left half of the chain corresponds to the x-component and the right half corresponds to the y-component.

erator admits a high degree of half-chain entanglement that grows with the propagation distance z. Assume that $f_x^2 + f_y^2 \ll \frac{1}{\lambda^2}$. Let $f^2 = f_x^2 + f_y^2$, $\epsilon = \left(\frac{2\pi}{k}\right)^2 f^2$ and $\sqrt{k^2 - (2\pi)^2 f^2} = k\sqrt{1 - \epsilon}$. Using a Taylor expansion $\sqrt{1 - \epsilon} \approx 1 - \frac{\epsilon}{2} + \ldots$, the propagator can be written as a product

$$\tilde{T}_z^{\text{Fresnel}}(f_x, f_y) = e^{izk} \tilde{T}_z(f_x) \tilde{T}_z(f_y),$$
 (17)

with $\tilde{T}_z(f) = \exp(-i\pi\lambda z f^2)$ and $T_z(x) = \frac{e^{ikz}}{i\lambda z} \exp(\frac{ik}{2z}x^2)$. We have shown that under the paraxial

approximation $f_x^2 + f_y^2 \ll \frac{1}{\lambda^2}$, the angular spectrum transfer function becomes separable (see Fig. 15). Using the operator notations we have $\hat{U}_{\text{Fresnel}} = \hat{U}_{\text{Fresnel}}^{(x)} \otimes \hat{U}_{\text{Fresnel}}^{(y)}$ and $\lim_{z\to 0} \hat{U}_{AS} = \hat{U}_{\text{Fresnel}}^{(x)} \otimes \hat{U}_{\text{Fresnel}}^{(y)}$.

Numerical simulations (see Fig. 17) suggest that lowrank representations of these operators might exist within the range of parameters we are working in. Both trans-

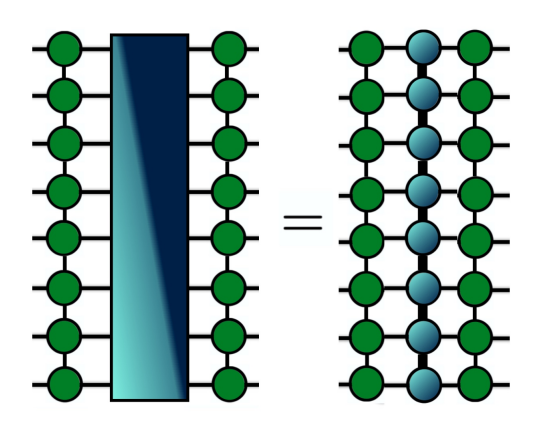


FIG. 18: MPO representation of the optical propagation as a product $\hat{U}_{\mathrm{QFT}}^{\dagger}\hat{U}(z)\hat{U}_{\mathrm{QFT}}$, with $\hat{U}(z)=\exp(-iz\hat{H})$ being a diagonal operator. The question is what is \hat{H} , both in the continuum and on a lattice.

fer functions are unitary and diagonal in Fourier space, which alone motivates us to construct discrete diagonal MPO representations by interpreting them as the unitary evolution (see Fig. 18) of free fermions on 1d lattices. In the following section, we focus on the 1d Fresnel propagator and systematically construct a low-rank MPO representation, drawing on an analogy with the evolution of a quantum free particle and its discretized spin-chain equivalent.

B. Fresnel propagator and the free quantum particle

As alluded to earlier, readers familiar with quantum mechanics 101 will readily notice the similarities between the Fresnel propagator and the unitary propagator of a non-relativistic quantum particle of mass m. For a free particle at position \vec{r} and momentum \vec{p} , the Hamiltonian is

$$\hat{\mathcal{H}}_{\text{free}} = \frac{\hat{p}^2}{2m} = \frac{\hbar^2 \hat{k}^2}{2m},\tag{18}$$

where $\hat{p} = \hbar \hat{k}$ and $\hat{k} = -i \partial_r$ in the position representation. The time-evolution operator (propagator) is

$$\hat{U}_{\text{free}}(t) = \exp\left(-\frac{i}{\hbar}\,\hat{\mathcal{H}}_{\text{free}}\,t\right).$$
 (19)

Momentum eigenstates $|k\rangle$ satisfy $\hat{k} |k\rangle = k |k\rangle$. Acting on such a state, the propagator yields in 2d

$$\hat{U}_{\text{free}}(t) |k\rangle = e^{-iE_k t/\hbar} |k\rangle, \qquad E_k = \frac{\hbar^2 (k_x^2 + k_y^2)}{2m}.$$
(20)

Equivalently, the momentum-space matrix elements are

$$\langle k | \hat{U}_{\text{free}}(t) | k' \rangle = e^{-iE_k t/\hbar} \delta(k - k').$$
 (21)

Thus, although \hat{k} is an operator in position space, in the momentum basis it is represented by its eigenvalue k, and the Hamiltonian (and therefore the propagator) becomes diagonal. Similarly, the 2d Fresnel transfer function describing paraxial wave propagation for wavelength λ over a transverse distance z is

$$\hat{U}_{\text{Fresnel}}(k,z) = \exp\left(-i\frac{\lambda(k_x^2 + k_y^2)}{4\pi}z\right). \tag{22}$$

This can be interpreted as a unitary evolution generated by the Hamiltonian

$$\hat{\mathcal{H}}_{\text{Fresnel}} = -\frac{\lambda}{4\pi} (\partial_x^2 + \partial_y^2), \tag{23}$$

so that $\hat{U}_{\text{Fresnel}}(z) = e^{-iz\hat{\mathcal{H}}_{\text{Fresnel}}}$. Thus, Fresnel propagation is formally analogous to the quantum evolution of a free-particle in one dimension, with the parameter identification

$$z \leftrightarrow t, \quad \frac{\lambda}{2\pi} \leftrightarrow \frac{\hbar}{m}.$$
 (24)

This similarity comes from the very well known equivalence between the Schrödinger equation and paraxial Helmholtz equations

$$\left(i\partial_z + \frac{\lambda}{4\pi}\partial_r^2\right)E = 0 \leftrightarrow \left(i\partial_t + \frac{\hbar}{2m}\partial_r^2\right)\psi = 0. \quad (25)$$

The addition of a potential V(x) in the former would imply a heterogenous refraction index n(x) in the later. As said earlier, the Fresnel/free particle propagator has, like the Fourier transform, a separable tensor product structure in space, so we can focus on its 1d discretization in the following.

1. Discretization of the Hamiltonian

Discretizing the 1d space into a lattice with L sites and spacing a, the second derivative operator is approximated by the discrete Laplacian

$$\left. \frac{\partial^2 \psi}{\partial x^2} \right|_i \approx \frac{\psi_{j+1} - 2\psi_j + \psi_{j-1}}{a^2}. \tag{26}$$

This corresponds to a tight-binding Hamiltonian on a one-dimensional chain

$$\hat{H} = -J \sum_{j=1}^{L-1} (|j\rangle \langle j+1| + |j+1\rangle \langle j|) + \mu \sum_{j=1}^{L} |j\rangle \langle j|,$$
(27)

with hopping strength $J = \lambda/4\pi a^2$ and onsite potential $\mu = \frac{\lambda}{2}$. Using fermionic operators c_j, c_j^{\dagger} for each site, with periodic boundary conditions $c_{L+1} \equiv c_1$, the Hamiltonian reads

$$\hat{H} = -J \sum_{j=1}^{L-1} \left(c_j^{\dagger} c_{j+1} + c_{j+1}^{\dagger} c_j \right) + \mu \sum_{j=1}^{L} c_j^{\dagger} c_j.$$
 (28)

Fourier transforming to momentum space diagonalizes the Hamiltonian

$$\hat{H} = \sum_{k} \epsilon(k) c_k^{\dagger} c_k, \tag{29}$$

with dispersion relation $\epsilon(k) = -2J\cos k + \mu$, $k \in [-\pi,\pi]$. Expanding near k=0 gives $\cos k \approx 1-\frac{k^2}{2} \to \epsilon(k) \approx -2J + Jk^2 + \mu$. Ignoring the constant shift $(-2J+\mu)$, the dispersion is approximately quadratic $\epsilon(k) \approx Jk^2$, which matches the continuous Fresnel dispersion by identifying $Ja^2 \leftrightarrow \frac{\lambda}{4\pi}$. In the following, we choose to keep the analysis at the level of the lattice with the oscillating dispersion as we could always take the parabolic limit in the end.

2. Hamiltonian in the qubit basis

Having wrote the Fresnel transform as the unitary propagation of a quantum Hamiltonian of L hopping particles on a lattice, we can proceed to compress the Hilbert space acting on $n = \log L$ qubits. Consider an n-qubit computational basis labeled by bitstrings $\mathbf{s} = (s_1, s_2, \ldots, s_n)$ where each $s_j \in \{0, 1\}$. Define the number $x_{\mathbf{s}} = \sum_{j=1}^n s_j 2^{-j} \in [0, 1)$, we then need to express the dispersion relation of the diagonalized Hamiltonian such that \hat{H} remains diagonal in the computational basis. Any diagonal hamiltonian (or operator for that matter) can be expanded in Pauli-strings of any size

$$\hat{H} = \sum_{S \subseteq \{1,\dots,n\}} c_S \prod_{j \in S} \hat{Z}_j, \tag{30}$$

where the coefficients are real and expressed as

$$c_{S} = \frac{1}{2^{n}} \operatorname{Tr} \left(\hat{H} \prod_{j \in S} \hat{Z}_{j} \right)$$

$$= \frac{1}{2^{n}} \sum_{\mathbf{s} \in \{0,1\}^{n}} \epsilon(\mathbf{s}) (-1)^{\sum_{j \in S} s_{j}}.$$
(31)

This decomposition is the Walsh–Hadamard transform (which is a generalized Fourier transform over the abelian group \mathbb{Z}_2^n), it can be computed very efficiently for large-system with the fast Walsh–Hadamard transform (see for example [45] and references within). Generally speaking, diagonal operators are crucially important in quantum computing as there are key elements of many quantum algorithms [46–49].

As a brief illustration of the method for n = 2. The possible Pauli-Z tensor products are

$$\{\mathbb{I} \otimes \mathbb{I}, \ Z \otimes \mathbb{I}, \ \mathbb{I} \otimes Z, \ Z \otimes Z\}.$$
 (32)

Suppose \hat{D} is diagonal with entries $\{d_0, d_1, d_2, d_3\}$, corresponding to basis states $\{|00\rangle, |01\rangle, |10\rangle, |11\rangle\}$. Then

$$c_a = \frac{1}{4} \sum_{x=0}^{3} d_x \chi_a(x), \quad a \in \{00, 01, 10, 11\},$$
 (33)

with $\chi_a(x) = (-1)^{a.x}$ for the group \mathbb{Z}_2^2 . This provides the coefficients for the decomposition $\hat{D} = \sum_{a \in \{0,1\}^2} c_a Z^a$.

In our specific case $\epsilon(\mathbf{s}) = \cos(2\pi x_{\mathbf{s}})$, a standard calculation (cf. appendix) gives the coefficients $c_S \in \mathbb{R}$ equal to

$$c_S = \frac{1}{2^n} \operatorname{Re} \left[\prod_{j=1}^n \left(1 + (-1)^{\mathbf{1}_{j \in S}} e^{i\theta_j} \right) \right],$$
 (34)

where we defined $\theta_j = \frac{2\pi}{2^j}$ and $S_1 = \hat{Z}_i$, $S_2 = \hat{Z}_i \hat{Z}_j$, $S_3 = \hat{Z}_i \hat{Z}_j \hat{Z}_k$ for $i, j, k \in [1, n]$ and so on. There is an exponentially large number of terms in the Pauli decomposition, but hopefully a finite number of them are contributing significantly to the sum. By separating the product over indices in S and not in S, we can write c_S as

$$c_S = \frac{1}{2^n} \operatorname{Re} \left(\gamma_n \prod_{j \in S} x_j \right), \tag{35}$$

with $\gamma_n = \frac{e^{i\pi\left(\frac{1}{2} - \frac{1}{2^n}\right)}}{\sin\left(\frac{\pi}{2^n}\right)}$ and $x_j = -i\tan(\theta_j/2)$. As n goes to infinity the Hamiltonian is made of absolutely convergent coefficients c_S . This hamiltonian, although made of Pauli-strings of any length at any distance, is effectively highly-local as n grows. Knowing that the two-body interactions are essentially limited to a few neighbors, what are the contributions coming from the longer strings of operators and what are their dependences to their relative size. Following this path, we traded the nearestneighbors fermionic hamiltonian Eq. (27) with L sites with a n-qubit system with exponentially decreasing interactions. This result relies heavily on the analyticity of the dispersion relation and is not expected to give a similar result in general [64]. Let us be more precise and compute the mean amplitude of Pauli-strings of size |S| = P

$$\bar{c}_P = \frac{1}{\binom{n}{P}} \sum_{|S|=P} c_S. \tag{36}$$

^[64] The Walsh-Fourier version of the Paley–Wiener theorem states that, for any finite abelian group, if $\epsilon(\mathbf{s})$ is analytic in a strip around the real line, then its Walsh–Fourier coefficients decay exponentially fast while smoothness alone would result in a polynomial decrease at best [50].

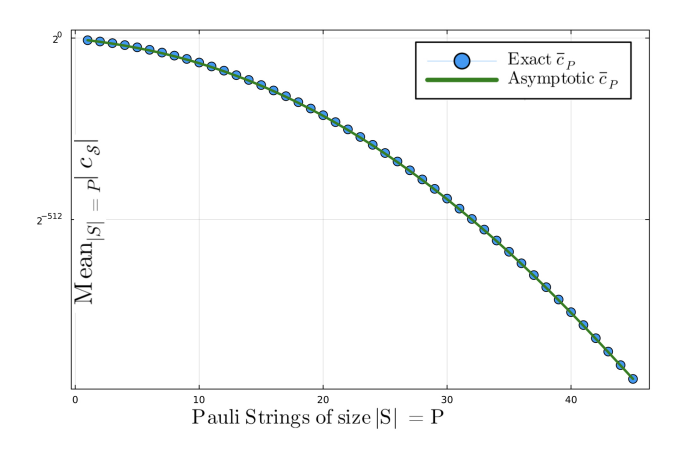


FIG. 19: Exponential decay of the mean amplitudes of Pauli strings of size P. The exact formula is given by Eq. (37) and the asymptotic by Eq. (39).

It is possible to compute the asymptotical behavior of the average amplitude of Pauli-strings. Indeed we can write \bar{c}_P as the coefficient of the generating function of all Paul-strings of size P.

$$\bar{c}_P = \frac{1}{2^n \binom{n}{P}} \operatorname{Re} \left[\gamma_n e_P(x_1, \dots, x_n) \right].$$
(37)

The elementary symmetric polynomial of degree P in n variables x_1, \ldots, x_n , well known in the context of the fractional quantum Hall effect [51] is defined as

$$e_P(x_1, \dots, x_n) = \sum_{1 \le j_1 < \dots < j_P \le n} x_{j_1} x_{j_2} \dots x_{j_P},$$
 (38)

and $e_0 = 1$ [65]. Thanks to the convergence properties of c_S , we can show (more details in the appendix) that the asymptotic behavior with respect to P is

$$\overline{c}_P \sim 2^{-P(P+1)/2} \left(\frac{\pi}{N}\right)^P P! \quad \text{for } P \ll n.$$
 (39)

This decay is super-exponential in P and it shows that the amplitudes of Pauli strings do not contribute at all past a certain string length. We plot in Fig. 19 this asymptotic behavior and compared it to the exact formula computed with the fast Walsch-Hadamard transform.

This asymptotic behavior is key to select a polynomially long sequence of gates that still retains machine precision and approximates the diagonal operator with an efficient MPO. If one truncates the Hamiltonian to include only Pauli strings of length P_m , the truncated unitary reads $\hat{U}_{\text{trunc}}(t) = e^{-it\hat{H}_{\text{trunc}}}$, with $\hat{H}_{\text{trunc}} = \sum_{|S| < P_m} c_S \hat{P}_S$. Since all terms commute, the truncation

[65] Actually, all the moments can be written using those polynomials, giving access to U(t) as an exact moment expansion.

error in operator norm can be bounded by the norm of the discarded tail Hamiltonian

$$\|\hat{U}(t) - \hat{U}_{\text{trunc}}(t)\| \le \|t\hat{H}_{\text{tail}}\|_{\text{op}} \le t \sum_{|S| > P_m} |\bar{c}_S|.$$
 (40)

Using the expression for \bar{c}_P , we get

$$\|\hat{U}(t) - \hat{U}_{\text{trunc}}(t)\| \lesssim t \sum_{P=P_m+1}^{n} {n \choose P} 2^{-P(P+1)/2} \left(\frac{\pi}{N}\right)^{P} P!.$$

Because the super-exponential decay $2^{-P(P+1)/2}$ dominates the combinatorial growth $\binom{n}{P}$ for moderate P, the truncation error decreases extremely rapidly with P, justifying the efficient approximation of $\hat{U}(t)$ by a sum of only short Pauli strings and giving access to a compact MPO representation using a polynomial $\mathcal{O}(n^{P_m})$ number of terms.

3. Unitary evolution, quantum circuit and MPO

Let us introduce the string operators $\hat{\mathbf{P}}_S = \prod_{j \in S} \hat{Z}_j$ such that $\hat{D} = \sum_{S \subseteq \{1,...,n\}} c_S \hat{\mathbf{P}}_S$. Each $\hat{\mathbf{P}}_S$ is Hermitian and unitary $\hat{\mathbf{P}}_S^{\dagger} = \hat{\mathbf{P}}_S$ and $\hat{\mathbf{P}}_S^2 = \hat{I}$ and different Pauli- \hat{Z} strings commute, $[\hat{\mathbf{P}}_S, \hat{\mathbf{P}}_{S'}] = 0$ for all S, S'. Because the terms in the hamiltonian commute pairwise, the exponential of the sum factorizes exactly into the product of exponentials, the unitary operator becomes

$$\hat{U}(t) = \prod_{S \subseteq \{1,\dots,n\}} e^{-ic_S t \hat{P}_S}.$$
(41)

Moreover, each factor $e^{-i\omega\hat{P}_S}$ has a closed form. Using the power-series definition of the exponential and separating even/odd powers, we obtain the elementary trigonometric form for the exponential operator

$$e^{-i\omega\hat{P}_S} = \cos(\omega)\hat{I} - i\sin(\omega)\hat{P}_S.$$
 (42)

Applying this with $\omega = c_S t$ gives each factor explicitly, therefore the exact evolution is

$$\hat{U}(t) = \prod_{S} \left[\cos(\omega) \hat{I} - i \sin(\omega) \hat{P}_{S} \right].$$
 (43)

This formula allows to construct a quantum circuit made only of CNOT and $R_z(2\omega)$ gates with coefficients $\{\omega\}$ given by Eq. (34). In Fig. 20, we illustrate a quantum circuit, with each n-qubit gates corresponding to a n-Pauli string in the decomposition. Because of the commutativity of the Pauli strings, the results are independent of the order of gates. The resulting matrix product operator is made by sequentially absorbing all the local tensors into an initial identity MPO. Numerically [66], we select

^[66] We can directly use native ITensor functions $U = \operatorname{apply}(\operatorname{ops}(\operatorname{\mathsf{gates}},\operatorname{\mathsf{qsites}}),\operatorname{MPO}(\operatorname{\mathsf{qsites}},"I";\operatorname{\mathsf{cutoff}} = 10^{-6}))$ where gates is a list of gates

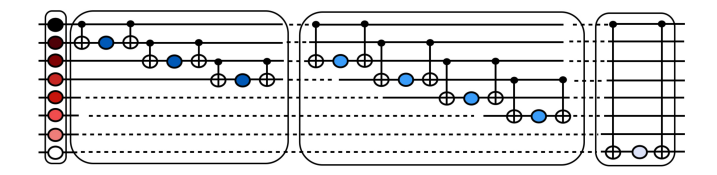


FIG. 20: Circuit representing the unitary evolution Eq. (43) made of only CNOT and R_z gates.

gates based on their amplitude and a cutoff at 10^{-6} is chosen, which is garanties a precision below 10^{-10} for the unitary. In Fig. 22, we plot the maximal rank of the

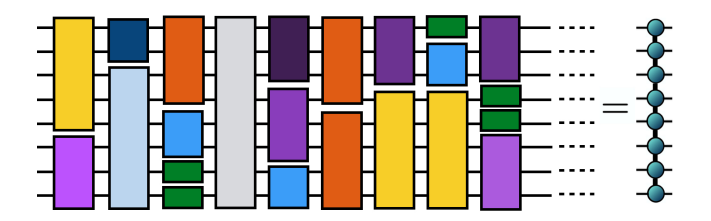


FIG. 21: Quantum circuit (Fig. 20) as a big tensor network and associated matrix product operator. The blocks of lengths P correspond to P-qubit gates. The order is irrelevant due to commutativity.

MPO up to n=20 and show that the entanglement saturates at a finite value when n grows which suggests that this diagonal operator is of finite-rank despite being constructed of an exponential number of Pauli-strings. Simi-

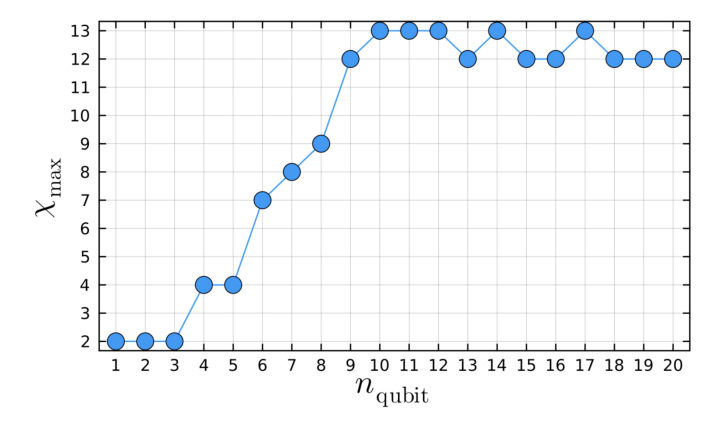


FIG. 22: Maximal rank of the MPO representing Fig. 21 when adding up all gates below 10^{-6} . The bond dimension $\chi_{\rm max}$ of the MPO saturates (for t=1) quickly when n grows, indicating a low-rank structure.

larly to the Fourier transform MPO, we have successfully showed that the Fresnel transform in Fourier space also admits a low rank structure in Fourier space. The real-space operator is also low-rank since it is a product of low-rank MPO (see Fig. 18). The numerical method developed here is very generic and is expected to work with any diagonal operator. Of course the maximal dimension

of the MPO will grow with the complexity of the function $\epsilon(\mathbf{s})$, but can always be controlled by truncating the terms in the Pauli expansion. As long as the behavior of \bar{c}_p is sufficiently decreasing, the quantum circuit and the MPO associated should stay numerically tractable for large value of n_{qubit} . Additionally, more subtle and efficient ways, such as recursive decomposition into multiplexed R_z gates [46, 52] allows to construct the MPO using $\mathcal{O}(n)$ gates. In the next section, we will introduce another method that is more mathematically explicit and offers some advantages in particular circumstances.

4. Closed-expression for the diagonal MPO using Bessel expansion

In this section, the goal is to write down a closed expression for a MPO representing the unitary evolution U(t) by using classical tools of statistical physics of spin systems. From this point of view, the diagonal unitary evolution operator

$$\hat{U}(t) = \sum_{\mathbf{s} \in \{0,1\}^n} e^{-it\epsilon(\mathbf{s})} |\mathbf{s}\rangle \langle \mathbf{s}|, \qquad (44)$$

with $\epsilon(\mathbf{s}) = \cos(2\pi \mathbf{s})$, correspond to the partition function of a classical 1d system with complex Boltzmann weights. A classical trick is to use the Jacobi-Anger expansion [53, 54], that states that for any $t \in \mathbb{R}$,

$$e^{-it\cos(2\pi\mathbf{s})} = \sum_{p=-\infty}^{\infty} (-i)^p J_p(t) e^{2i\pi p\mathbf{s}}$$

$$= \sum_{p=-\infty}^{\infty} (-i)^p J_p(t) \prod_{j=1}^n e^{ips_j\theta_j}, \qquad (45)$$

with $\theta_j = \frac{2\pi}{2^j}$ and where $J_p(t)$ is the p-th Bessel function of the first kind. The last formula is directly a matrix product operator as a superposition of plane waves weighted by Bessel-function coefficients. In practice, the infinite sum over p is truncated to $|p| \leq p_{\text{max}}$. Let $\chi = 2p_{\text{max}} + 1$ be the bond dimension, corresponding to the p index. Define local tensors W_j with physical index s_j and bond indices $p_{\text{in}}, p_{\text{out}}$ as

$$[W_j]_{p_{\text{in}},p_{\text{out}}}^{s_j} = \begin{cases} e^{ip_{\text{in}}\theta_j s_j}, & p_{\text{out}} = p_{\text{in}} \\ 0, & \text{otherwise} \end{cases}, \tag{46}$$

with $p_{\rm in}, p_{\rm out} \in \{-p_{\rm max}, \dots, p_{\rm max}\}$. The left and right boundary vectors $|v^R\rangle, |v^L\rangle \in \mathbb{C}^\chi$ are defined by their components

$$\begin{cases} v_p^L = (-i)^p J_p(t) \\ v_p^R = 1. \end{cases}$$
 (47)

The bond dimension $\chi = 2p_{\text{max}} + 1$ corresponds directly to the number of retained Fourier modes in the truncated

expansion. Then the MPO contraction reproduces $\hat{U}(t)$ in an exact closed-form

$$\hat{U}(t) = \sum_{\mathbf{s}} \left(\langle v^L | W_1^{s_1} W_2^{s_2} ... W_n^{s_n} | v^R \rangle \right) |\mathbf{s}\rangle \langle \mathbf{s}|.$$
 (48)

To evaluate the convergence of the matrix product operator representation, we define the truncated expansion

$$\hat{U}_{p_{\text{max}}} = \sum_{p=-p_{\text{max}}}^{p_{\text{max}}} (-i)^p J_p(t) \prod_{j=1}^n e^{iks_j \theta_j}, \qquad (49)$$

and monitor the successive difference

$$\delta(p_{\text{max}}) = \max \left| \hat{U}_{p_{\text{max}}} - \hat{U}_{p_{\text{max}}-1} \right|. \tag{50}$$

Since the phase factors $\prod_{j=1}^{n} e^{ipb_j\theta_j}$ have unit modulus,

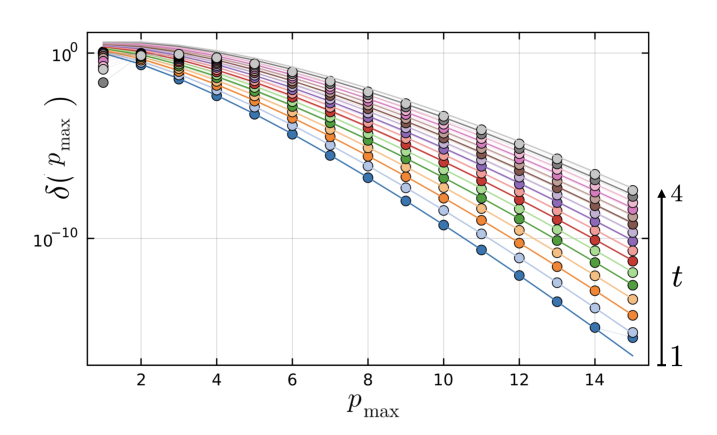


FIG. 23: Exponential convergence of the Bessel MPO for increasing values of $t \in [1, 4]$, the solid lines correspond to the asymptotic estimate for n = 12.

the truncation error satisfies $\delta(p_{\max}) \leq \sum_{|p|>p_{\max}} |J_p(t)|$. Using the bound $|J_p(t)| \leq \frac{|t|^p}{p!}$, valid for all $p \in \mathbb{Z}$, we obtain the asymptotic estimate $\delta(p_{\max}) \lesssim \frac{|t/2|^{p_{\max}}}{(p_{\max})!}$, which decays super-exponentially with p_{\max} . Numerical simulations confirm that for fixed n the sequence $\delta(p_{\max})$ rapidly decreases as p_{\max} grows, with decay rates consistent with the asymptotic Bessel bound. In particular, plotting $\delta(p_{\max})$ on a logarithmic scale for times $t=1,2,\ldots,10$ shows excellent agreement between the exact convergence behavior and the analytical estimate. In Fig. 24, we show how the MPO converges toward the exact unitary matrix very quickly, at $p_{\max}=14$ the operator errors $\epsilon(p_{\max})$ are well below 10^{-10} for all reasonable sizes available to our computer. The same Bessel bound used above gives also an exponential scaling $\epsilon(p_{\max}) \lesssim \frac{|t|^{p_{\max}}}{(p_{\max})!}$ up to floating-point roundoff.

C. Angular spectrum propagator as a free relativistic quantum particle

Now we consider the natural generalization of the free Hamiltonian in the case of relativistic quantum mechan-

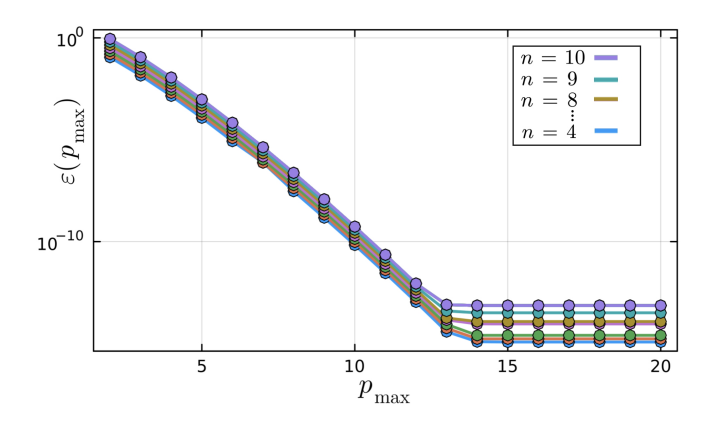


FIG. 24: Unitary matrix reconstruction error for n = 4, 5, ..., 10 and t = 1. The error decreases exponentially fast and remain constant for a finite value of k_{max} .

ics. The full (non-paraxial) Helmholtz equation Eq. (16) maps directly to the 1 + 1d Klein-Gordon equation,

$$(\Box + m^2)\psi = 0, (51)$$

which is known to lead to a non-local Hamiltonian (square-root of the Laplacian) when interpreted as first-order equation. In order to obtain a proper local Hamiltonian, which can be discretize on a lattice, we can follow the Dirac interpretation of the square-root laplacian [55].

This section will not be as detailed as the previous section and we will only highlight the main points of the calculations. We consider a 1d lattice with L sites and spacing a. At each site $n=1,\ldots,L$ we place a two-component spinor

$$\hat{\psi}_i = \begin{pmatrix} \hat{\psi}_{i,1} \\ \hat{\psi}_{i,2} \end{pmatrix}, \tag{52}$$

with second-quantized fermion operators obeying $\{\hat{\psi}_{n,\alpha}, \hat{\psi}^{\dagger}_{m,\beta}\} = \delta_{nm}\delta_{\alpha\beta}$ and $\{\gamma^{\mu}, \gamma^{\nu}\} = 2\eta^{\mu\nu}I$, $\mu, \nu = 0, 1$, with $\eta = \text{diag}(1, -1)$ with $(\gamma^0)^2 = I$, $(\gamma^1)^2 = -I$, $\{\gamma^0, \gamma^1\} = 0$. We discretize the derivative in the free Dirac Hamiltonian

$$\hat{\mathcal{H}}_{\text{free}}^{\text{rel}} = -i\hbar c \hat{X} \hat{\partial}_x + mc^2 \hat{Z},\tag{53}$$

using the symmetric finite difference

$$\partial_x \psi_n \to \frac{\psi_{n+1} - \psi_{n-1}}{2a}.\tag{54}$$

This yields the discrete Dirac Hamiltonian [67]

$$\hat{H} = -\frac{i\hbar c}{2a} \sum_{n} (\hat{\psi}_{n}^{\dagger} \hat{X} \hat{\psi}_{n+1} + \text{h.c.}) + mc^{2} \sum_{n} \hat{\psi}_{n}^{\dagger} \hat{Z} \hat{\psi}_{n}, \quad (55)$$

^[67] The infamous fermion doubling problem will not pose a significant problem in our context

with periodic boundary conditions $\psi_{L+1} \equiv \psi_1$. The equation becomes block-diagonal in momentum space

$$\hat{H} = \sum_{k} \Psi_k^{\dagger} \hat{H}(k) \Psi_k, \qquad \hat{H}(k) = \frac{\hbar c}{a} (\sin k) \hat{X} + mc^2 \hat{Z}.$$
(56)

Let $|u_k^{\pm}\rangle$ denote the corresponding normalized eigenvectors. The exact propagator in momentum space is

$$U(t) = e^{-i\hat{H}(k)t/\hbar} = V_k \operatorname{diag}\left(e^{-i\epsilon_k^+ t/\hbar}, e^{-i\epsilon_k^- t/\hbar}\right) V_k^{-1},$$
(57)

where $V_k = (|u_q^+\rangle, |u_q^-\rangle)$ collects eigenvectors. If we select one eigensubspace, say the negative-energy branch (and drop the - subscript), then the Hamiltonian acts as a scalar on that subspace

$$\hat{H}(k)|u_k\rangle = \epsilon_k |u_k\rangle, \qquad \hat{U}(t)|u_k\rangle = e^{-i\epsilon_k t/\hbar} |u_k\rangle, (58)$$

with

$$\epsilon(k) = \sqrt{\left(\frac{\hbar c}{a}\sin(ka)\right)^2 - m^2c^4}.$$
 (59)

For small $ka \ll 1$, the dispersion becomes (posing $\hbar c = 1$)

$$\epsilon(k) = \sqrt{k^2 - m^2},\tag{60}$$

recovering the continuum relation of the energy of a relativistic particle of mass m. Similarly to the previous section, we can identify this propagator as the angular spectrum transfer function by choosing the right parameter identification $\hbar k \leftrightarrow mc$ and $\hbar k_x \leftrightarrow p$. In the following, we choose again to stay in the lattice Eq. (59) as we could always take the continuum limit in then end.

A similar calculation to the previous non-relativistic case can be carried out by following the same steps. The qubit Hamiltonian writes in Fourier space

$$\hat{H} = \sum_{\mathbf{s}} \epsilon(\mathbf{s}) |\mathbf{s}\rangle \langle \mathbf{s}| = \sum_{S \subset \{1, \dots, n\}} c_S \prod_{j \in S} \hat{Z}_j, \qquad (61)$$

with

$$\epsilon(\mathbf{s}) = \sqrt{1 - \beta^2 \sin^2(2\pi x_\mathbf{s})}.\tag{62}$$

Introducing the angle $\varphi_{\mathbf{s}} = 2\pi x_{\mathbf{s}}$. Since the function $\epsilon(\mathbf{s})$ is even and π -periodic, it admits a Fourier-cosine expansion

$$\sqrt{1 - \beta^2 \sin^2 \varphi} = a_0(\beta) + \sum_{\mu=1}^{\infty} a_{\mu}(\beta) \cos(2\mu\varphi), \quad (63)$$

with Fourier coefficients

$$a_0(\beta) = \frac{1}{\pi} \int_0^{\pi} d\varphi \sqrt{1 - \beta^2 \sin^2 \varphi},$$

$$a_{\mu}(\beta) = \frac{2}{\pi} \int_0^{\pi} d\varphi \sqrt{1 - \beta^2 \sin^2 \varphi} \cos(2m\varphi) \quad \mu \ge 1.$$
(64)

In that case the formula for the coefficient of the Paulistring decomposition is

$$c_S = \frac{1}{2^n} \sum_{\mu=0}^{\infty} a_{\mu}(\beta) \operatorname{Re} \left[\prod_{j=1}^n \left(1 + (-1)^{\mathbf{1}_{j \in S}} e^{i\theta_j^{(\mu)}} \right) \right], (65)$$

where $\theta_j^{(\mu)} = \frac{\mu 4\pi}{2^j}$. The first integral is equal to $a_0(\beta) = (1/\pi)E(\pi,\beta)$ with E being the incomplete elliptic integral of the second kind and the second integral can be expressed in terms of hypergeometric functions

$$a_{\mu} = (1 + \gamma^{-1}) \frac{(-\frac{1}{2})_{\mu}(-\lambda^{2})^{\mu}}{\mu!} {}_{2}F_{1}\left(-\frac{1}{2}, \mu - \frac{1}{2}; \mu + 1; \lambda^{4}\right),$$

for $\mu \ge 1$ with $\gamma^{-1} = \sqrt{1-\beta^2}$, and $(a)_{\mu} = a(a+1)(a+2)\cdots(a+\mu-1)$ and where $\lambda = \beta/(1+\gamma^{-1})$. For fixed μ , the integrals converge absolutely. As $\mu \to \infty$, a_{μ} decays exponentially because the function $\sqrt{1-\beta^2\sin^2\phi}$ is analytic in a strip around the real axis since $0 < \beta < 1$. Because of the exponentially decreasing behavior of the Pauli string coefficients, the MPO also admits a very lowrank representation. We do not show the quantum unitary circuit or the MPO implementation, as they closely mirror the Fresnel propagator. In this study, the dispersion relations are analytic functions of k implying exponentially fast decrease of their Hadamard coefficients. Mathematically it sounds reasonable to assert that any Hamiltonian with an analytic/holomorphic dispersion relation should admit a low-rank MPO representation. It would be very important to precisely quantify this behavior more rigorously for a larger class of functions. Alternatively, a similar Bessel-type expansion can also be found in this case, leading to a closed expression for this MPO, although we do not show details here as they do not add value to the discussion.

Additionally, it would be informative to compare the rank of the resulting MPO with that obtained from a more TCI-based implementation. Also, another quantum-inspired method, which does not rely on the Fourier transform, has been recently developed [56] to solve quantum free evolution. Such comparisons, along with more realistic applications, will be the subject of future research. Surprisingly enough, although we have dealt with two operators that are diagonalizable by Fourier transform, we did not construct the Fourier transform MPO by this method as its associated Hamiltonian $\hat{\mathcal{H}} = \frac{1}{2}(\hat{p}^2 + \hat{x}^2)$ is not diagonalizable by Fourier transform (as \hat{H} is not translational invariant), but rather by the basis of discrete Hermite functions. It would be very interesting to calculate an MPO representation using this Hamiltonian formulation and compare with [37].

VI. CONCLUSIONS AND PERSPECTIVES

Over the years, tensor networks have become highly efficient at simulating complex quantum systems, and re-

searchers have only recently begun to explore their potential in other fields such as numerical simulations, optimization, and machine learning. In this work, we demonstrated how tensor networks can be highly effective in image processing, thanks to their remarkable compression capabilities.

We showed how Fourier optics can be cast as a form of quantum mechanics, with qubits whose evolution is dictated by unitary operators that can be represented as matrix product operators, allowing efficient computations. In the future, we plan to extend this work to broader optical applications and explore algorithms for optical inverse problems—such as phase retrieval, denoising, and deconvolution—which have numerous applications in astronomy, earth observation, and microscopy.

Acknowledgements I am deeply grateful to Bernhard Jobst for discussions in the early stage of this paper, and to all the contributors to the ITensor library ecosystem [57]. All simulations have been carried out on a 2015 macbook pro 16GB.

- [1] R. J. Baxter, Journal of Mathematical Physics 9, 650 (1968).
- [2] S. R. White, Physical review letters **69**, 2863 (1992).
- [3] H.-L. Huang, W.-S. Bao, and C. Guo, Physical Review A 100, 032305 (2019).
- [4] C. Oh, M. Liu, Y. Alexeev, B. Fefferman, and L. Jiang, arXiv preprint arXiv:2306.03709 (2023).
- [5] M. Liu, C. Oh, J. Liu, L. Jiang, and Y. Alexeev, Physical Review A 108, 052604 (2023).
- [6] J. Tindall, M. Fishman, M. Stoudenmire, and D. Sels, arXiv preprint arXiv:2306.14887 (????).
- [7] S. Patra, S. S. Jahromi, S. Singh, and R. Orús, Physical Review Research 6, 013326 (2024).
- [8] E. Stoudenmire and D. J. Schwab, Advances in neural information processing systems 29 (2016).
- [9] I. Glasser, N. Pancotti, and J. I. Cirac, arXiv preprint arXiv:1806.05964 p. 50 (2018).
- [10] R. D. Peddinti, S. Pisoni, A. Marini, P. Lott, H. Argentieri, E. Tiunov, and L. Aolita, Communications Physics 7, 135 (2024).
- [11] L. Arenstein, M. Mikkelsen, and M. Kastoryano, arXiv preprint arXiv:2505.17046 (2025).
- [12] N.-L. van Hülst, P. Siegl, P. Over, S. Bengoechea, T. Hashizume, M. G. Cecile, T. Rung, and D. Jaksch, arXiv preprint arXiv:2507.05222 (2025).
- [13] N. Gourianov, P. Givi, D. Jaksch, and S. B. Pope, Science Advances 11, eads5990 (2025).
- [14] L. Hölscher, P. Rao, L. Müller, J. Klepsch, A. Luckow, T. Stollenwerk, and F. K. Wilhelm, Physical Review Research 7, 013112 (2025).
- [15] S. Rihito, T. Haruto, and M. Koichi, Mathematics 13, 1828 (2025).
- [16] K. Lively, V. Pagni, and G. Camacho, arXiv preprint arXiv:2504.11181 (2025).
- [17] S. H. Hauck, M. Kabel, M. Ali, and N. R. Gauger, arXiv preprint arXiv:2412.11566 (2024).
- [18] N. Jolly, Y. N. Fernández, and X. Waintal, Physical Review B 111, 245115 (2025).
- [19] J. I. Latorre, arXiv preprint quant-ph/0510031 (2005).
- [20] R. Dilip, Y.-J. Liu, A. Smith, and F. Pollmann, Physical Review Research 4, 043007 (2022).
- [21] B. Jobst, K. Shen, C. A. Riofrío, E. Shishenina, and F. Pollmann, Quantum 8, 1544 (2024).
- [22] D. L. Ruderman, Network: computation in neural systems 5, 517 (1994).
- [23] D. L. Ruderman, Vision research 37, 3385 (1997).

- [24] P. Q. Le, F. Dong, and K. Hirota, Quantum Information Processing 10, 63 (2011).
- [25] G. Cataldi, A. Abedi, G. Magnifico, S. Notarnicola, N. Dalla Pozza, V. Giovannetti, and S. Montangero, Quantum 5, 556 (2021).
- [26] R. Oberdorf, A. Ferguson, J. L. Jacobsen, and J. Kondev, Physical Review E—Statistical, Nonlinear, and Soft Matter Physics 74, 051801 (2006).
- [27] I. Oseledets, in *Doklady Mathematics* (Springer, 2009), vol. 80, pp. 653–654.
- [28] B. N. Khoromskij, Constructive Approximation 34, 257 (2011).
- [29] S. Wiesner, arXiv preprint quant-ph/9603028 (1996).
- [30] C. Zalka, Proceedings of the Royal Society of London. Series A: Mathematical, Physical and Engineering Sciences 454, 313 (1998).
- [31] J. C. Bridgeman and C. T. Chubb, Journal of physics A: Mathematical and theoretical 50, 223001 (2017).
- [32] J. Biamonte and V. Bergholm, arXiv preprint arXiv:1708.00006 (2017).
- [33] R. Orús, Nature Reviews Physics 1, 538 (2019).
- [34] S. Montangero, E. Montangero, and Evenson, *Introduction to tensor network methods* (Springer, 2018).
- [35] M. Collura, G. Lami, N. Ranabhat, and A. Santini, Tensor network techniques for quantum computation (2024).
- [36] J. Tindall, M. Stoudenmire, and R. Levy, arXiv preprint arXiv:2410.03572 (2024).
- [37] J. Chen, E. Stoudenmire, and S. R. White, PRX Quantum 4, 040318 (2023).
- [38] J. Chen and M. Lindsey, arXiv preprint arXiv:2404.03182
- [39] J. W. Goodman, *Introduction to Fourier optics* (Roberts and Company publishers, 2005).
- [40] E. Stoudenmire and S. R. White, New Journal of Physics 12, 055026 (2010).
- [41] A. J. Ferris and G. Vidal, Physical Review B—Condensed Matter and Materials Physics 85, 165146 (2012).
- [42] M. K. Ritter, Y. Núñez Fernández, M. Wallerberger, J. von Delft, H. Shinaoka, and X. Waintal, Physical Review Letters 132, 056501 (2024).
- [43] Y. Núñez Fernández, M. K. Ritter, M. Jeannin, J.-W. Li, T. Kloss, T. Louvet, S. Terasaki, O. Parcollet, J. von Delft, H. Shinaoka, et al., SciPost Physics 18, 104 (2025).
- [44] A. A. Michailidis, C. Fenton, and M. Kiffner, arXiv preprint arXiv:2410.19747 (2024).

- [45] T. N. Georges, B. K. Berntson, C. Sünderhauf, and A. V. Ivanov, New Journal of Physics 27, 033004 (2025).
- [46] S. S. Bullock and I. L. Markov, arXiv preprint quantph/0303039 (2003).
- [47] S. S. Bullock and I. L. Markov, arXiv preprint quantph/0303039 (2008).
- [48] J. Welch, D. Greenbaum, S. Mostame, and A. Aspuru-Guzik, New Journal of Physics 16, 033040 (2014).
- [49] Y. Nakata and M. Murao, The European Physical Journal Plus 129, 152 (2014).
- [50] W. Rudin, Fourier analysis on groups (Courier Dover Publications, 2017).
- [51] I. G. Macdonald, Symmetric functions and Hall polynomials (Oxford university press, 1998).
- [52] V. V. Shende, S. S. Bullock, and I. L. Markov, in Proceedings of the 2005 Asia and South Pacific Design Au-

- tomation Conference (2005), pp. 272-275.
- [53] Y. Liu, Y. Meurice, M. Qin, J. Unmuth-Yockey, T. Xiang, Z. Xie, J. Yu, and H. Zou, Physical Review D—Particles, Fields, Gravitation, and Cosmology 88, 056005 (2013).
- [54] A. Samlodia, V. Longia, R. G. Jha, and A. Joseph, Physical Review D 110, 034504 (2024).
- [55] P. A. M. Dirac, Proceedings of the Royal Society of London. Series A, Containing Papers of a Mathematical and Physical Character 117, 610 (1928).
- [56] J. Gidi, P. García-Molina, L. Tagliacozzo, and J. J. García-Ripoll, Journal of Computational Physics 539, 114228 (2025).
- [57] M. Fishman, S. White, and E. M. Stoudenmire, SciPost Physics Codebases p. 004 (2022).

Appendix A: Pauli string exact formula

We derive an exact expansion of the function

$$\cos\left(2\pi\sum_{j=1}^{n}s_{j}2^{-j}\right),\tag{A1}$$

where each $s_j \in \{0,1\}$ represents a binary digit. We express this function in terms of Pauli-Z operators acting on an n-qubit Hilbert space and give an explicit formula for the expansion coefficients. We discuss properties of this expansion, its convergence in the thermodynamic limit, and implications for approximations in quantum many-body systems. Consider an n-qubit computational basis labeled by bitstrings $\mathbf{s} = (s_1, s_2, \dots, s_n)$ where each $s_j \in \{0, 1\}$. Define the number

$$x_{\mathbf{s}} = \sum_{j=1}^{n} s_j 2^{-j} \in [0, 1).$$
 (A2)

We want to express the function $f(\mathbf{s}) = \cos(2\pi x_{\mathbf{s}}) = \cos\left(2\pi \sum_{j=1}^{n} s_{j} 2^{-j}\right)$ as an operator diagonal in the computational basis $\hat{F} = \sum_{\mathbf{s}} f(\mathbf{s}) |\mathbf{s}\rangle \langle \mathbf{s}|$. Recall the single-qubit Pauli-Z operator acts as $Z|0\rangle = |0\rangle$ and $Z|1\rangle = -|1\rangle$. For n qubits, define operators

$$Z_j = I^{\otimes (j-1)} \otimes Z \otimes I^{\otimes (n-j)}, \tag{A3}$$

acting non-trivially only on qubit j. A convenient operator basis for diagonal operators on n qubits is the set of all products $\prod_{j \in S} Z_j$, where $S \subseteq \{1, 2, ..., n\}$. For the empty set $S = \emptyset$, the product is the identity operator $I^{\otimes n}$. These operators satisfy

$$\left(\prod_{j\in S} Z_j\right) |\mathbf{s}\rangle = (-1)^{\sum_{j\in S} s_j} |\mathbf{s}\rangle. \tag{A4}$$

Therefore, any diagonal operator can be expanded as

$$\hat{F} = \sum_{S \subseteq \{1,\dots,n\}} c_S \prod_{j \in S} Z_j,\tag{A5}$$

with coefficients $c_S \in \mathbb{R}$. Because the operators $\prod_{j \in S} Z_j$ are diagonal and orthogonal under the Hilbert-Schmidt inner product, the coefficients can be extracted by

$$c_S = \frac{1}{2^n} \sum_{\mathbf{s} \in \{0,1\}^n} f(\mathbf{s}) (-1)^{\sum_{j \in S} s_j}.$$
 (A6)

Inserting $f(\mathbf{s}) = \cos\left(2\pi \sum_{j=1}^{n} s_j 2^{-j}\right)$, we get

$$c_S = \frac{1}{2^n} \sum_{\mathbf{s}} \cos \left(2\pi \sum_{j=1}^n s_j 2^{-j} \right) (-1)^{\sum_{j \in S} s_j}$$
(A7)

$$= \operatorname{Re} \left[\frac{1}{2^n} \sum_{s} e^{i2\pi \sum_{j=1}^n s_j 2^{-j}} (-1)^{\sum_{j \in S} s_j} \right]$$
(A8)

$$= \operatorname{Re} \left[\frac{1}{2^n} \prod_{j=1}^n \sum_{s_j=0}^1 e^{i2\pi s_j 2^{-j}} (-1)^{s_j \mathbf{1}_{j \in S}} \right]. \tag{A9}$$

Each sum over s_j is

$$\sum_{s_{i}=0}^{1} e^{i2\pi s_{j} 2^{-j}} (-1)^{s_{j} \mathbf{1}_{j \in S}} = 1 + (-1)^{\mathbf{1}_{j \in S}} e^{i\theta_{j}}, \tag{A10}$$

where we defined $\theta_j = \frac{2\pi}{2^j}$. Hence

$$c_S = \frac{1}{2^n} \operatorname{Re} \left[\prod_{j=1}^n \left(1 + (-1)^{\mathbf{1}_{j \in S}} e^{i\theta_j} \right) \right].$$
(A11)

The coefficient c_S factorizes as a product of simple two-term factors. For $j \notin S$, the factor is $1 + e^{i\theta_j}$ and for $j \in S$, the factor is $1 - e^{i\theta_j}$. Since $\theta_j = \frac{2\pi}{2^j}$ decreases exponentially with j, the terms involving high j contribute less. The coefficients c_S decay quickly in magnitude as |S| increases or as the indices j in S grow. As $n \to \infty$,

$$\hat{D} = \sum_{S \subseteq \mathbb{N}} c_S \prod_{j \in S} \hat{Z}_j, \tag{A12}$$

is an infinite series with absolutely convergent coefficients c_S because

$$|1 \pm e^{i\theta_j}| \approx \sqrt{2 - 2\cos\theta_j} \sim \theta_j \sim 2^{-j} \to 0. \tag{A13}$$

This allows efficient approximations by truncation to low-order subsets S, making it useful for matrix product operator (MPO) approximations in quantum many-body systems. We have derived a compact exact formula for the Pauli-Z expansion coefficients of the function.

Unitary evolution

We start from an operator given by a diagonal expansion in Pauli-Z strings,

$$D = \sum_{S \subseteq \{1,\dots,n\}} c_S P_S, \qquad P_S \equiv \prod_{j \in S} Z_j, \tag{A14}$$

and derive the exact form of the time-evolution operator $U(t) = e^{-iHt}$. Because all P_S commute and satisfy $P_S^2 = I$, the unitary factorizes and each factor has a simple closed form. We give the derivation, show the action on the computational basis, and briefly discuss practical consequences. Let n be the number of (spin-1/2) sites. Denote by Z_j the Pauli-Z operator acting on site j (identity elsewhere). Each P_S is Hermitian and unitary

$$P_S^{\dagger} = P_S, \qquad P_S^2 = I, \tag{A15}$$

and different Pauli-Z strings commute, because every Z_i is diagonal and $Z_iZ_j=Z_jZ_i$ for all i,j

$$[P_S, P_{S'}] = 0 \quad \text{for all } S, S'. \tag{A16}$$

We want the time-evolution operator $U(t) = e^{-iDt}$. Because the terms commute pairwise, the exponential of the sum factorizes exactly into the product of exponentials

$$U(t) = \prod_{S \subseteq \{1, \dots, n\}} e^{-ic_S t P_S}.$$
 (A17)

Moreover, each factor $e^{-i\theta P_S}$ has a closed form because $P_S^2 = I$. Using the power-series definition of the exponential and separating even/odd powers,

$$e^{-i\theta P_S} = \sum_{k=0}^{\infty} \frac{(-i\theta)^k}{k!} P_S^k = \sum_{m=0}^{\infty} \frac{(-1)^m \theta^{2m}}{(2m)!} I - i \sum_{m=0}^{\infty} \frac{(-1)^m \theta^{2m+1}}{(2m+1)!} P_S,$$
(A18)

we obtain the elementary trigonometric form

$$e^{-i\theta P_S} = \cos(\theta) I - i\sin(\theta) P_S. \tag{A19}$$

Applying this with $\theta = c_S t$ gives each factor explicitly. Therefore the exact evolution is

$$U(t) = \prod_{S} \left(\cos(c_S t) I - i \sin(c_S t) P_S \right). \tag{A20}$$

Exact derivation of the mean amplitude of Pauli-Z coefficients by subset size

We can rewrite c_S by separating the product over indices in S and not in S

$$c_S = \frac{1}{2^n} \operatorname{Re} \left[\prod_{j \in S} (1 - e^{i\theta_j}) \prod_{j \notin S} (1 + e^{i\theta_j}) \right]$$
(A21)

$$= \frac{1}{2^n} \operatorname{Re} \left[\left(\prod_{j>1} (1 + e^{i\theta_j}) \right) \prod_{j \in S} \frac{1 - e^{i\theta_j}}{1 + e^{i\theta_j}} \right], \tag{A22}$$

for j > 1. Only subsets S that contain qubit 1 $(C_S = 0 \text{ for } 1 \notin S)$ give nonzero coefficients. Define

$$x_j = \frac{1 - e^{i\theta_j}}{1 + e^{i\theta_j}} = -i\tan(\theta_j/2),\tag{A23}$$

so that

$$c_S = \frac{1}{2^n} \operatorname{Re} \left[\left(\prod_{j>1} (1 + e^{i\theta_j}) \right) \prod_{j \in S} x_j \right]. \tag{A24}$$

The mean coefficient over all strings of size P is then

$$\overline{c}_P = \frac{1}{\binom{n}{P}} \sum_{|S|=P} c_S = \frac{1}{2^n \binom{n}{P}} \operatorname{Re} \left[\left(\prod_{j>1} (1 + e^{i\theta_j}) \right) \sum_{|S|=P} \prod_{j \in S} x_j \right]. \tag{A25}$$

Recognizing the sum over products as the elementary symmetric polynomial $e_P(x_1,\ldots,x_n)$, we obtain

$$\overline{c}_{P} = \frac{1}{2^{n} \binom{n}{P}} \operatorname{Re} \left[\left(\prod_{j>1} (1 + e^{i\theta_{j}}) \right) e_{P}(x_{1}, \dots, x_{n}) \right]
= \frac{1}{2^{n} \binom{n}{P}} \operatorname{Re} \left[\left(\frac{e^{i\pi \left(\frac{1}{2} - \frac{1}{2^{n}}\right)}}{\sin \left(\frac{\pi}{2^{n}}\right)} \right) e_{P}(x_{1}, \dots, x_{n}) \right],$$
(A26)

with $x_j = -i \tan(\theta_j/2)$. The elementary symmetric polynomial of degree P in n variables x_1, \ldots, x_n is defined as

$$e_P(x_1, \dots, x_n) = \sum_{1 < j_1 < j_2 < \dots < j_P < n} x_{j_1} x_{j_2} \dots x_{j_P}, \quad e_0 = 1.$$
(A27)

For large n and $P \ll n$, the θ_j for j > P are small and contribute negligibly to the elementary symmetric polynomial. Therefore, the polynomial is dominated by the first P terms

$$e_P(x_1, \dots, x_n) \sim \prod_{j=1}^P x_j = \prod_{j=1}^P (-i \tan(\theta_j/2)).$$
 (A28)

Using $\theta_i/2 = \pi/2^j$, we have

$$\prod_{j=1}^{P} \tan(\theta_j/2) \sim \prod_{j=1}^{P} \frac{\pi}{2^j} = \pi^P \, 2^{-P(P+1)/2}. \tag{A29}$$

The product of cosines in the prefactor converges to a constant $C = \prod_{j=1}^{\infty} \cos(\pi/2^j)$, and the division by $\binom{n}{P} \sim n^P/P!$ yields

$$\bar{c}_P \sim P! C \pi^P 2^{-P(P+1)/2} n^{-P}, \text{ for } P \ll n.$$
 (A30)

Thus, the coefficients decay exponentially in P(P+1)/2 and polynomially in n, illustrating the rapid decrease of contributions from large strings.